Automated Finite Element Modeling of Staggered Composites: Software Framework, Verification, and Architectural Effects

Raúl Muñoz[a,*], Carlos Izquierdo-Martín[a], Sebastián Andrés Toro[b]

[a]*Department of Mechanical Engineering, University of Salamanca, Plaza de los Caídos s/n, Salamanca, 37008, Spain*
[b]*Departamento de Ingeniería Mecánica, Universidad de Santiago de Chile, USACH, Av. Bernardo O'Higgins 3363, Santiago, Chile*

Abstract

This study presents a parametric Python framework to automate two-dimensional finite element model generation of staggered brick-and-matrix composites in Abaqus/Standard. The suite includes four standalone scripts—for periodic and finite-gauge tensile models, double-cantilever beam (DCB), and three-point end-notched flexure (3ENF) specimens—with three complementary plug-ins that generate editable, native Abaqus/CAE databases. User-defined parameters govern key geometric variables (brick length, ply count, layer offset), material assignments, cohesive interfaces, precracks, boundary conditions, and mesh discretization, facilitating systematic architectural evaluations. To ensure numerical robustness, an analysis of potential numerical artifacts, mesh sensitivity, and the validity of an RVE representation within a highly non-linear regime was conducted. Given the mesh dependency of Hashin damage evolution, several postprocessing criteria based on damage initiation were evaluated alongside published experimental data to determine the optimal mesh size. Using this calibrated setup,

*Corresponding author.
Email addresses: raul.munoz@usal.es (Raúl Muñoz), sebastian.toro@usach.cl (Sebastián Andrés Toro)

the framework was deployed to analyze the mechanical effects of brick length and layer offset. Architectural comparisons showed that aligned matrix pockets produced the lowest tensile stiffness and load capacity, while a quarter-pitch offset achieved the highest tensile stiffness and strength among non-aligned configurations. Interestingly, the best-performing tensile configuration did not provide the best fracture performance, revealing a fundamental trade-off between tensile and fracture resistance.
Keywords: Staggered composites, Finite element automation, Abaqus, Mesh sensitivity, Hashin damage, Delamination

1. Introduction

Fibre-reinforced polymer composites are widely used in aerospace, wind-energy, automotive, rail and civil-engineering structures because they combine high specific stiffness and strength with durability and corrosion resistance. However, composites lack the capacity to redistribute stresses through plastic deformation, making them less damage-tolerant to stress concentrations, flaws, and local impacts than metallic materials [1, 2]. To enhance damage tolerance, strategies such as fibre hybridisation, interleaving, and through-thickness reinforcement have been extensively investigated [3–7].

Staggered, or brick-and-matrix, architectures offer a compelling bio-inspired alternative derived from nacre. Discontinuous stiff bricks are separated by a more compliant matrix, and axial load is transferred between neighbouring bricks partly by matrix shear. This arrangement effectively redistributes stresses, arrests crack propagation, and alters damage localization paths [8–11]. Extensive research demonstrates that brick length, matrix-pocket geometry, loading direction, layer arrangement, and interface morphology strongly govern stiffness, strength, and fracture resistance [12–19].

A comprehensive mechanical characterization of staggered composites requires evaluating both axial performance and delamination resistance. Uniaxial tensile tests quantify stiffness, non-linearity, and ultimate strength, whereas Mode I double-cantilever beam (DCB) and Mode II three-point end-notched flexure (3ENF) tests evaluate opening- and shear-dominated interlaminar fracture [20, 21]. Both regimes are critical when introducing staggered architectures into structural repairs. However, experimentally screening every combination of brick geometry, overlap offset, layer count, and constituent interface properties requires a prohibitively large manufacturing and testing campaign.

Finite element (FE) analysis offers a scalable alternative, yet manual model construction in commercial software remains labor-intensive and prone to user error. Modifying architectural parameters—such as brick length, matrix-pocket size, or ply stacking—forces the manual reconstruction of geometry, partitions, material assignments, meshing, sets, surfaces, interactions, and boundary conditions. Furthermore, periodic tensile unit cells require compatible boundary meshes and multi-point constraints, while DCB and 3ENF models demand meticulous setup of non-linearly interacting contact surfaces, cohesive zone properties, and traction-free pre-cracks.

These simulations are also computationally challenging. Matrix plasticity and ductile damage continuously interact with cohesive delamination, crack-face contact, and potential intralaminar failure modes. While implicit solvers avoid the small stable time increments of explicit quasi-static schemes, abrupt stiffness degradation and contact status changes frequently cause convergence failures or severe cutbacks. Artificial damping techniques, such as automatic static stabilization and cohesive viscosity, improve solver robustness but risk dissipating excessive artificial energy, which can alter predicted peak loads and fracture paths [22–24]. Consequently, artificial energy metrics must be rigorously monitored and controlled.

Tensile modeling also introduces domain-size dependencies. Although periodic unit cells are computationally efficient and support non-linear boundary conditions [25], post-peak damage localization presents a challenge: a single cell forces failure patterns to repeat periodically, potentially suppressing damage modes whose characteristic wavelength exceeds the unit cell domain [26–28]. The validity of a periodic representative volume element (RVE) must therefore be benchmarked against full finite-gauge specimens across the non-linear response.

To address these challenges, this work introduces *Staggering*, a Python framework for automated two-dimensional tensile, DCB, and 3ENF finite element modeling of staggered composites in Abaqus/Standard. The suite features four standalone scripts that generate complete, execution-ready `.inp` files without launching a graphical user interface, alongside three Abaqus/CAE plug-ins that produce native, fully editable `.cae` databases. Both pathways instantiate model entities directly from a unified set of physical parameters, eliminating redundant manual setup and ensuring strict geometric and boundary consistency across parametric studies.

2. Software organisation and modelling capabilities

2.1. Scripts and generation routes

Figure 1 illustrates the architecture of *Staggering* categorized by test family and generation route. Two complementary execution pathways are available: standalone Python scripts and Abaqus/CAE plug-ins.

The standalone scripts generate complete Abaqus input files (`.inp`) relying strictly on the Python standard library, supporting both Python 2.7 and Python 3. Because model generation operates independently of the Abaqus/CAE GUI, no GUI license is consumed, rendering this pathway ideal for automated command-line parameter sweeps and reproducible simulation campaigns. An

Abaqus/Standard solver license is subsequently required to execute the resulting analyses.

The Abaqus/CAE plug-ins utilize the Abaqus Scripting Application Programming Interface (API) to construct native parts, partitions, section assignments, interactions, steps, meshes, and job definitions. The generated model databases (`.cae`) remain fully interactive, enabling visual inspection, manual post-processing, or custom feature modifications. This suite was developed and verified on Abaqus 2018.

Both generation routes support tensile, double-cantilever beam (DCB), and three-point end-notched flexure (3ENF) finite element models. For tensile loading, users can specify either a longitudinally periodic unit cell or a finite-gauge specimen subject to uniform axial displacement. Table 1 summarizes the available entry points and their corresponding output models.

Table 1: Overview of *Staggering* script entry points and primary generated output models.

Test	Standalone Python entry point	Native plug-in	Output model
Tension	`generate_tensile_periodic_inp.py`; `generate_tensile_uniform_inp.py`	`StaggeringTensile`	Longitudinally periodic cell or finite-gauge model with uniform end displacement
DCB	`generate_dcb_inp.py`	`StaggeringDCB`	Mode I specimen with precrack and user-selected candidate interfaces
3ENF	`generate_3enf_inp.py`	`Staggering3ENF`	Mode II specimen, precrack, supports, and central indenter

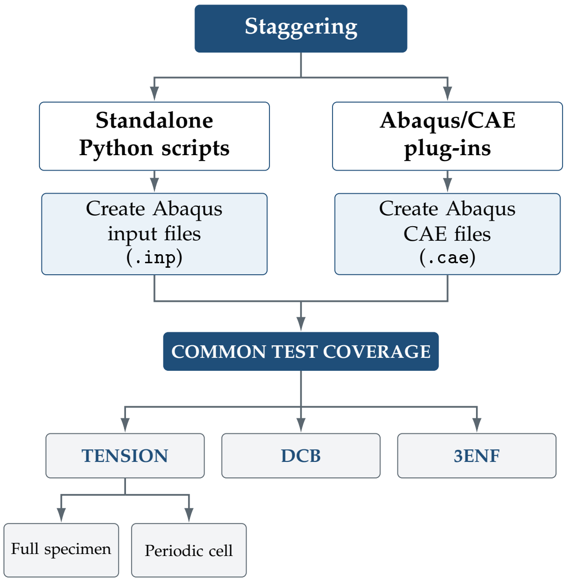

Figure 1: Generation pathways and test coverage of *Staggering*. Standalone Python scripts write raw Abaqus input files, whereas Abaqus/CAE plug-ins build native, editable CAE databases. Both routes accommodate tension, DCB, and 3ENF configurations; the tensile module includes both finite-gauge and longitudinally periodic formulations.

2.2. *Modelling approach and capabilities of each script*

2.2.1. *Script workflow*

For every script, the analyst specifies the fundamental geometric parameters: brick length L_{brick}, matrix-pocket length L_{matrix}, ply thickness t, ply count n, total modelled length, and individual layer offsets. The longitudinal pitch p is defined as

$$p = L_{\mathrm{brick}} + L_{\mathrm{matrix}}. \tag{1}$$

Layer offsets can be prescribed as non-dimensional fractions of p or specified independently for each ply. Furthermore, the generators accommodate a continuous-ply baseline reference by removing the longitudinal matrix pockets while preserving specimen dimensions, interlayer interfaces, boundary/loading conditions, and pre-crack configurations.

Model generation commences with input parameter validation, followed by the explicit calculation of brick–matrix interface boundaries, layer offsets, and test-specific spatial coordinates. These coordinates define distinct material domains and establish a fully structured mesh whose element boundaries align strictly with material transitions. The framework then assigns section properties, brick material orientations, cohesive interfaces, boundary conditions, solver controls, and field output requests before writing the execution-ready input file or saving the native CAE database. Consequently, modifying architectural parameters automatically regenerates all geometric partitions and mesh distributions.

The framework provides comprehensive control over numerical settings, including geometric non-linearity (`NLGEOM`), unsymmetric matrix storage, automatic time-incrementation parameters, and explicit output time points. Independent controls govern damage initiation, progressive damage evolution, cohesive viscosity, and automatic static-step stabilization. In addition, normal and shear cohesive stiffnesses (K_{nn}, K_{ss}, and K_{tt}) are treated as independent input parameters. These numerical capabilities are deployed for the benchmark studies detailed in Section 3, where specific input values are systematically documented.

2.2.2. Longitudinally periodic tensile cell

The script `generate_tensile_periodic_inp.py` generates the material-scale periodic tensile model depicted in Figure 2(a). Each ply comprises one or more complete brick-and-matrix periods. Discontinuous bricks are modeled as orthotropic unidirectional domains incorporating Hashin damage initiation and optional energy-based damage evolution. The matrix is represented as an isotropic elastoplastic material with optional ductile damage, while surface-based cohesive interactions govern the interfaces between adjacent plies. A plane-stress formulation is adopted to maintain compatibility with the built-in Abaqus Hashin damage failure criteria [32].

Longitudinal periodic boundary conditions (PBCs) are enforced via kinematic constraint equations according to

$$u_1^{\mathrm{R}} - u_1^{\mathrm{L}} = U_1^{\mathrm{macro}}, \qquad u_2^{\mathrm{R}} - u_2^{\mathrm{L}} = 0, \tag{2}$$

where R and L denote paired boundary nodes on the right and left periodic edges, respectively, and $U_1^{\mathrm{macro}} = u_1^{\mathrm{RP}}$ represents the prescribed macroscopic displacement applied at a dedicated control reference point. To eliminate rigid-body translation without suppressing transverse Poisson contraction, a single node near the midpoint of the bottom boundary is pinned ($u_1 = u_2 = 0$).

The script accommodates both a single unit cell and multi-period supercell domains. Standardized field and history output requests are automatically configured for reference-point displacement and reaction forces, constituent damage state variables, cohesive-interface traction/separation fields, and global energy balance histories. These outputs provide the macroscopic stress–strain response and

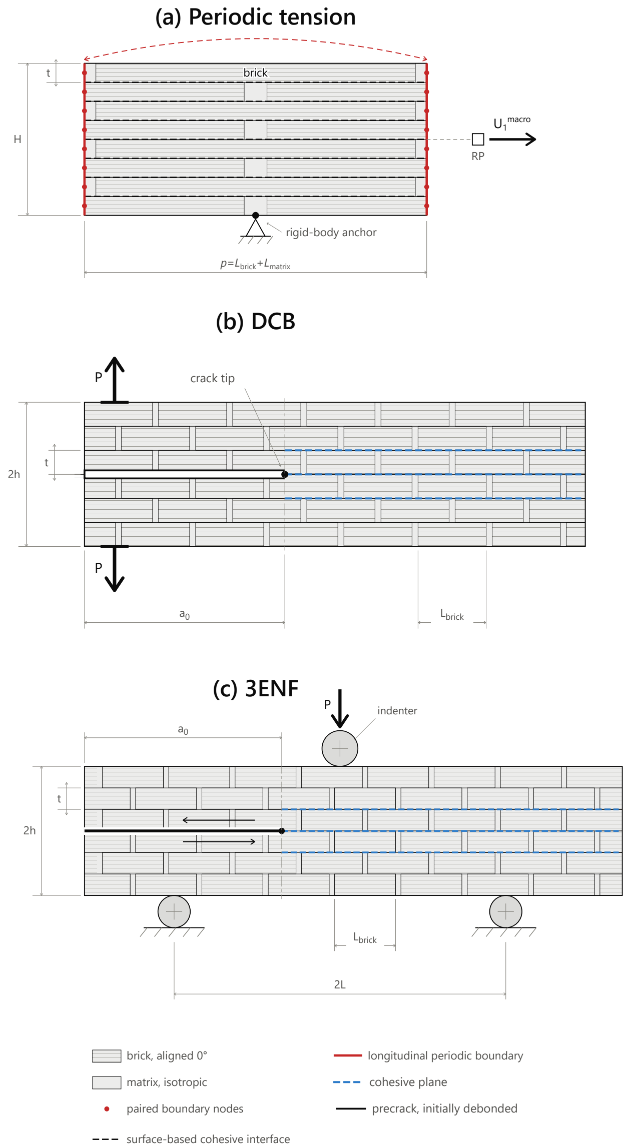

Figure 2: Finite element model schematics generated by *Staggering*: (a) longitudinally periodic tensile cell, (b) DCB specimen, and (c) 3ENF specimen. In (a), red boundaries denote paired periodic nodes, $p = L_{\text{brick}} + L_{\text{matrix}}$, t represents ply thickness, n is the ply count, and total height $H = nt$. In (b) and (c), a_0 indicates the initial pre-crack length, while blue dashed lines designate candidate cohesive crack propagation paths.

localized stress fields necessary to evaluate damage initiation, progressive failure, and artificial numerical dissipation.p

2.2.3. Finite-gauge tensile specimen

Although periodic boundary conditions accommodate non-linear constitutive behaviour [29], localized damage and cohesive softening can lead to strain localization and a loss of unit-cell representativeness [30]. Enforcing periodic boundary constraints inherently restricts admissible kinematic deformation patterns; thus, geometric periodicity alone does not guarantee that a unit cell accurately reproduces the progressive failure mechanics of a finite specimen [31].

To evaluate these domain-size dependencies, the script `generate_tensile_uniform_inp.py` generates a finite-gauge tensile model utilizing identical architectural parameters, constitutive formulations, and mesh discretization procedures as the periodic cell. Uniform longitudinal displacements applied at the specimen ends replace periodic boundary conditions. The underlying architecture can be repeated along the gauge length to match physical specimen dimensions, allowing strain localization and failure modes to evolve unconstrained across multiple architectural periods without enforcing kinematic periodicity on the solution.

2.2.4. Double cantilever beam

The script `generate_dcb_inp.py` constructs the Mode I DCB specimen depicted in Figure 2(b). Equal and opposite transverse displacements prescribed at reference points drive symmetric opening of the two arms, yielding a total separation of $\delta = 2|U_2|$, where the reaction force at either control node defines the applied load. Discontinuous bricks retain their orthotropic constitutive description, whereas the matrix accommodates elastoplastic deformation with optional ductile damage. Standardized output requests for interface elements facilitate tracking of cohesive process zone development ahead of the pre-crack tip.

The crack geometry and candidate propagation pathways are governed by three primary parameters: the initial pre-crack length a_0, the interface index hosting the pre-crack, and a user-defined set of candidate fracture interfaces. These inputs collectively define the crack-tip coordinate and the ply boundaries along which delamination can propagate or migrate. Modifying any parameter automatically regenerates the corresponding geometric partitions, surface definitions, and contact/cohesive interactions.

Each candidate interface comprises two opposing surfaces partitioned at $x = a_0$. On the pre-cracked interface, the region behind the crack tip ($x < a_0$) is initially unbonded and assigned hard normal contact with frictionless tangential behaviour, preventing crack-face interpenetration without transmitting cohesive tractions. Ahead of the tip ($x \geq a_0$), surface-based cohesive behavior models the intact ligament. Hard normal contact remains active following cohesive degradation to transfer compressive forces upon crack closure.

For secondary candidate interfaces, the region behind $x = a_0$ is joined via node-to-surface tie constraints, while the region ahead receives the same cohesive formulation to provide alternative delamination paths. To prevent over-constraint and solver singularities, boundary nodes at $x = a_0$ are explicitly assigned to cohesive surface definitions and excluded from tie constraints. Non-candidate interfaces remain permanently bonded either through shared nodes where meshing is conforming, or through full-length tie constraints between independently meshed domains.

This partitioning strategy also permits localized mesh refinement within the plies adjacent to the pre-crack without forcing globally refined element grids. For each tie constraint, the generator automatically designates the coarser mesh discretization as the master surface and constructs non-overlapping set definitions for tied, cohesive, and contact-only domains. This architecture is shared by both the standalone generator and the Abaqus/CAE plug-in.

Linear or exponential cohesive softening laws can be selected. Furthermore, viscous regularization (cohesive viscosity) and automatic static-step stabilization can be adjusted independently.

2.2.5. Three-point end-notched flexure

The script `generate_3enf_inp.py` constructs the Mode II shear-dominated fracture specimen shown in Figure 2(c). It inherits the architectural layout, pre-crack controls, and candidate interface logic from the DCB formulation, while introducing two analytical rigid support rollers and a central loading indenter. Fixture geometry is governed by user-defined roller radii and span positions.

Finite-sliding surface-to-surface contact models the interaction between the specimen and rigid fixtures. Analytical rigid entities serve as master surfaces; hard normal contact prevents boundary penetration, while penalty-based tangential contact accounts for roller–specimen friction. The pre-crack interface retains the frictionless crack-face contact formulation described for the DCB model. Reaction forces and vertical displacements recorded at the indenter reference node yield the macroscopic load–displacement curve, while cohesive interface state variables and global energy histories enable detailed monitoring of shear crack propagation and numerical dissipation.

3. Numerical assessment

The framework was deployed to conduct tensile mesh-sensitivity studies, evaluate the validity of the longitudinally periodic unit cell, and perform global energy balance checks to establish the numerical reliability and physical limitations of predicted responses. Systematic mesh refinement quantifies the discretization sensitivity of damage initiation and maximum stress, whereas comparisons against finite-gauge specimens assess whether a periodic cell adequately captures progressive damage localization. Furthermore, energy balance monitoring quantifies artificial numerical damping and viscous dissipation. Together, these benchmarks justify the selected working model and define the response range over which subsequent architectural trade-offs can be interpreted.

Reference geometries, material properties, cohesive parameters, mesh specifications, and solver controls are detailed in Appendix A. Case-specific parameter variations are documented within the corresponding studies.

3.1. Mesh sensitivity and initiation-only failure indicators

The periodic tensile module was applied to a reference cell featuring 10 mm bricks and 0.5 mm matrix pockets. Four spatial discretizations, designated e2, e4, e6, and e8, incorporate two, four, six, and eight elements through the thickness of each ply, corresponding to nominal element heights of 0.070, 0.035, approximately 0.0233, and 0.0175 mm, respectively. All constituent material and interface parameters were held constant across these meshes. Predictions from progressive Hashin damage simulations are benchmarked against initiation-only post-processing criteria and published experimental test data [19].

3.1.1. Mesh sensitivity with and without Hashin damage evolution

Mesh sensitivity was evaluated by comparing full progressive failure simulations against an initiation-only formulation. The progressive model incorporates stiffness degradation and viscous regularization during damage evolution, whereas the initiation-only variant evaluates Hashin initiation criteria without enacting subsequent softening.

Tensile strength was determined from the maximum macroscopic stress in the progressive model and from the stress corresponding to the first full-ply connected initiation event in the initiation-only model (evaluated using the post-processing criteria detailed in Section 3.1.2). Truncating the response curve at this initiation event establishes a consistent, initiation-based strength indicator across meshes without altering constitutive equations or introducing softening-induced mesh dependencies.

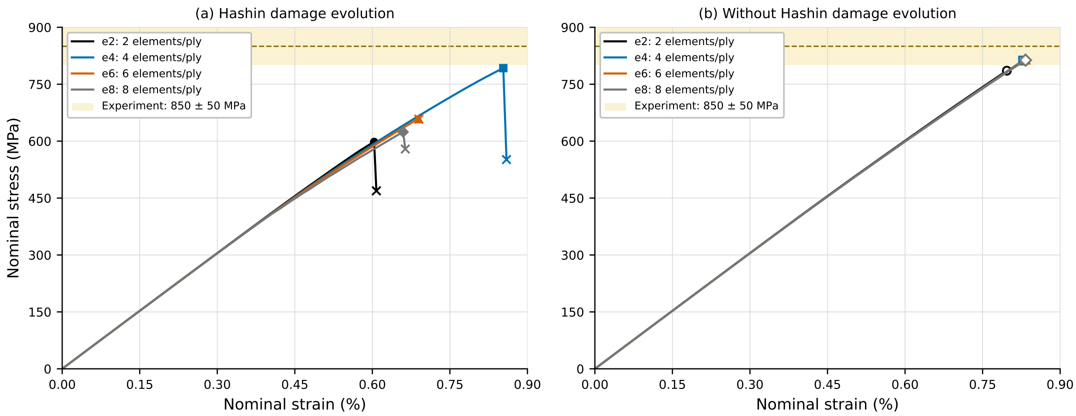

Figure 3: Mesh sensitivity of the 10 mm-brick periodic tensile cell across e2, e4, e6, and e8 meshes: (a) progressive Hashin damage evolution and (b) Hashin initiation without post-peak stiffness degradation. Filled symbols designate progressive stress maxima, crosses indicate the final converged increments, and open symbols denote the full-ply connected initiation event. The dashed line and shaded band represent the experimental mean and standard deviation (850 ± 50 MPa) [19].

As shown in Figure 3, the mechanical responses of all four meshes coincide prior to damage initiation. However, once progressive Hashin damage evolution is activated, the predicted ultimate strength exhibits severe mesh dependency. Peak computed stresses are 597.9, 792.5, 658.0, and 624.2 MPa for e2, e4, e6, and e8, respectively, displaying a non-monotonic dependence on mesh refinement.

In contrast, the initiation-only calculations evaluated via the full-ply connected criterion exhibit marked numerical stability. The corresponding event stresses are 785.7, 812.4, 814.8, and 813.5 MPa—a variation range of approximately 29 MPa (3.6% relative to e4). This confirms that initiation-based indicators provide mesh-converged failure estimates. However, because initiation-only calculations omit damage evolution, they cannot capture post-peak stress redistribution or residual load-bearing capacity resulting from progressive intralaminar failure.

Comparing progressive damage predictions with experimental measurements (850 ± 50 MPa) [19] yields relative errors of -29.7%, -6.8%, -22.6%, and -26.6% for e2, e4, e6, and e8, respectively. The e4 discretization (0.035 mm element height, four elements per 0.14 mm ply) provides the closest agreement with experimental data, lying just 7.5 MPa below the lower experimental bound. Consequently, the e4 mesh is selected as the baseline discretization for subsequent comparisons. It should be emphasized that this choice represents an experimentally informed working discretization for the specific material system and geometry considered, rather than a generally applicable or formally mesh-converged solution.

3.1.2. Initiation-only failure indicators

To identify spatially coherent fibre-tension failure onset from initiation-only calculations, two non-local post-processing methodologies were developed: connected-band criteria and an enriched-ply criterion. Both strategies operate strictly on stored output databases without altering finite element equations or introducing constitutive damage softening.

The *connected-band approach* groups active brick elements satisfying `HSNFTCRT` $\geq$ 0.95 into contiguous spatial components within a given ply. Connectivity requires a shared complete element edge. Active components must contain at least two elements and span at least 25%, 50%, or 99% of the ply thickness to qualify as quarter-, half-, or full-ply failure events, respectively. A custom Python script scans stored Abaqus output frames, identifies the earliest frame satisfying the given spatial threshold, records the corresponding macroscopic stress and strain, and truncates the reported response curve at that point.

The *enriched-ply criterion* evaluates damage initiation over a fixed physical characteristic domain. The post-processor reconstructs a spatial screening index from the 2D Hashin fibre-tension expression:

$$F_{\mathrm{ft},j} = \left(\frac{\langle \sigma_{11,j} \rangle_+}{X_\mathrm{T}}\right)^2 + \alpha \left(\frac{\tau_{12,j}}{S_\mathrm{L}}\right)^2, \tag{3}$$

where $\langle \cdot \rangle_+$ denotes the positive part (Macaulay brackets) and $\alpha = 1.0$. For tensile axial stress ($\sigma_{11} \geq 0$), Equation (3) matches the standard undegraded Hashin criterion. Under compressive axial stress ($\sigma_{11} < 0$), the post-processor isolates the shear contribution, serving strictly as a tensile screening index.

This point-wise index is spatially averaged around element i using a kernel weighting function:

$$\overline{F}_{\mathrm{ft},i}(R) = \frac{\displaystyle\sum_{j \in \mathcal{N}_i(R)} A_j \left[1 - (r_{ij}/R)^2\right]^2 F_{\mathrm{ft},j}}{\displaystyle\sum_{j \in \mathcal{N}_i(R)} A_j \left[1 - (r_{ij}/R)^2\right]^2}, \tag{4}$$

where A_j is the element area and r_{ij} represents the distance between element centroids. The neighborhood $\mathcal{N}_i(R)$ includes only elements within characteristic radius R that reside within the same ply and connected brick region. Periodic distance metrics are enforced across longitudinal cell boundaries. Damage initiation is defined by the first interpolated state where $\max_i \overline{F}_{\mathrm{ft},i} = 1.0$. The characteristic radius is fixed to the ply thickness ($R = t = 0.14$ mm) during mesh refinement.

Figure 4 compares these four initiation criteria across mesh densities. The quarter-ply criterion shows step-like sensitivity due to the discrete row counts required to satisfy its span threshold. Conversely, the enriched-ply prediction exhibits exceptional convergence, shifting by only 4.6 MPa (778.5 to 773.9 MPa) between e2 and e8.

Across all evaluated brick lengths and meshes, the half-ply and full-ply criteria trigger in identical output frames, yielding identical event stresses. This concur-

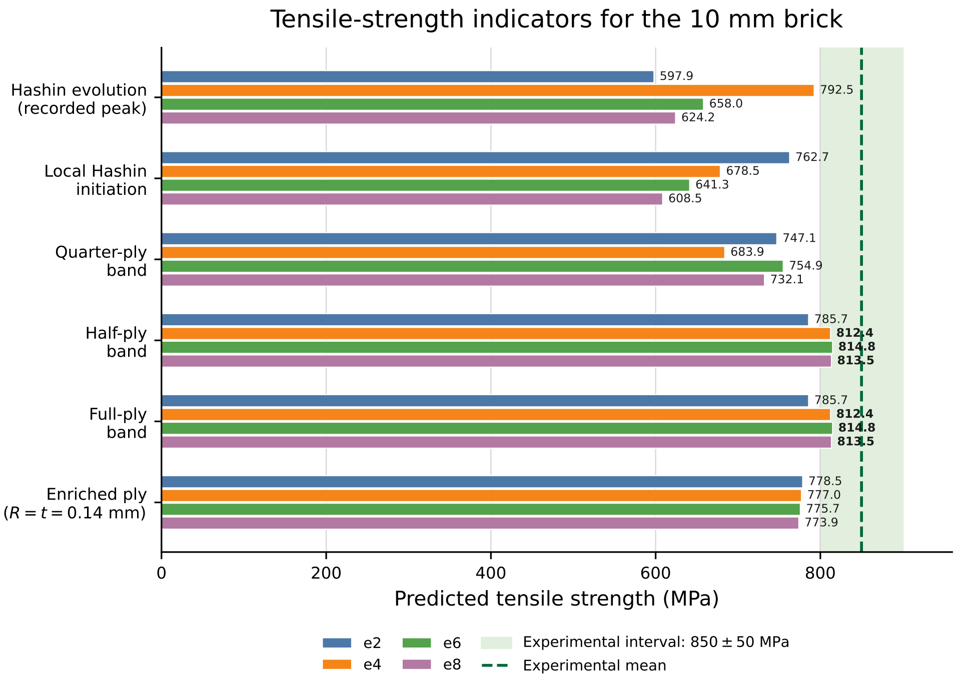

Figure 4: Comparison of ply-scale tensile strength indicators for the 10 mm-brick cell across e2–e8 meshes. The shaded band and dashed line represent the experimental range (850 ± 50 MPa) and mean [19]; bold labels mark predictions falling within this experimental interval. Un-averaged local initiation and progressive peak stresses are included for baseline comparison.

rence indicates rapid transverse growth of the damaged zone relative to frame output intervals rather than theoretical equivalence between the two definitions.

Table 2 summarizes mesh sensitivity (defined as the stress range across e2–e8 normalized by the e4 value) and experimental agreement (measured via mean absolute percentage error, MAPE, relative to experimental means across 10, 25, and 50 mm brick lengths).

Table 2: Mesh sensitivity and experimental error of ply-scale damage initiation post-processing criteria.

Criterion	Relative mesh range (%)			e4 MAPE (%)
	10 mm	25 mm	50 mm	10/25/50 mm
Quarter ply	10.38	9.94	10.62[a]	15.99
Half ply	3.59	3.62	3.89	12.93
Full ply	3.59	3.62	3.89	12.93
Enriched ply, $R = t$	0.60	0.45	0.37	13.88

[a] The 50 mm quarter-ply range incorporates e2–e6 because the e8 event was unrecorded; all other criteria evaluate e2–e8.

The enriched-ply criterion achieves superior mesh independence across all brick lengths ($< 0.60\%$ variation). However, the half- and full-ply criteria achieve lower overall experimental MAPE (12.93%). Selection depends on study objectives: connected-ply criteria offer closer absolute agreement with physical test data, whereas the spatially averaged enriched-ply measure provides maximum objectivity against mesh refinement.

3.2. Assessment of the periodic cell against a finite-gauge specimen

The computationally efficient one-period longitudinally periodic cell was compared with an 84.5 mm finite-gauge specimen containing eight periods and uniformly coupled ends. Both models use the e4 local discretization and the constituent, interface, and progressive Hashin parameters detailed in Tables A.2 and A.3. The target nominal strain is 1.2%, corresponding to axial extensions of 0.126 mm for the periodic cell and 1.014 mm for the finite gauge. This comparison evaluates whether the single-period domain reproduces key elastic and pre-peak response metrics; it serves as a consistency check between boundary formulations rather than an independent physical validation.

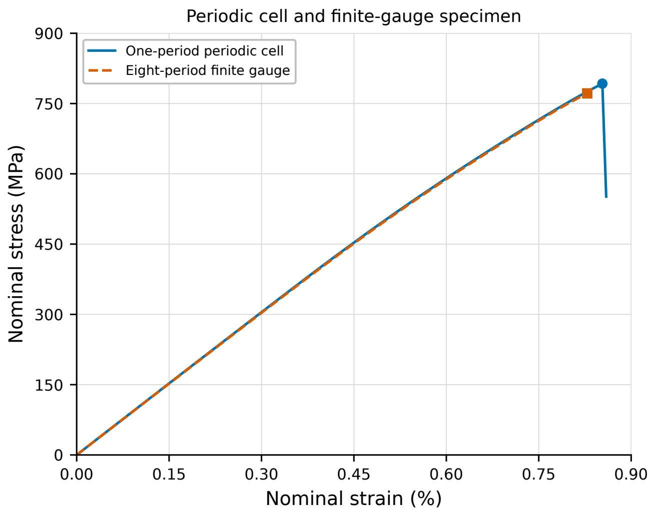

Figure 5: Nominal stress–strain response of the one-period longitudinally periodic tensile cell compared against the eight-period finite-gauge specimen.

The periodic cell yields an initial elastic modulus of 101.83 GPa and a maximum stress of 792.47 MPa at 0.853% strain. The corresponding finite-gauge values are 101.40 GPa and 771.67 MPa at 0.829% strain. Relative to the periodic unit cell, the finite-gauge modulus, peak stress, and strain at maximum stress are lower by 0.42%, 2.63%, and 2.88%, respectively. Furthermore, Hashin matrix-tension initiation occurs at an identical nominal strain of 0.324% in both models.

These minor discrepancies confirm that a single periodic cell accurately captures elastic stiffness, pre-peak non-linearity, and damage initiation for this deterministic architecture. However, periodic boundary conditions enforce artificial damage periodicity during post-peak degradation, suppressing domain-scale damage localization. Consequently, a full finite-gauge specimen or an enlarged supercell remains necessary when studying post-peak softening, defect sensitivity, or boundary-induced stress concentrations.

3.3. Numerical energy assessment

Implicit finite element convergence is frequently challenged in these models by non-linear interactions among matrix plasticity, severe damage-induced stiffness loss, and evolving contact boundary conditions. Abrupt damage propagation or cohesive interface failure can trigger repeated time-increment cutbacks or complete solver stagnation. Although unsymmetric matrix storage and tailored solver controls enhance robustness, viscous regularization or automatic static stabilization is often required to maintain numerical stability. Because excessive dissipation can distort predicted structural responses, all associated numerical energy components are continuously monitored throughout the loading range.

Three regularization mechanisms may be active depending on the simulation type:

1. Hashin damage viscosity, regularizing intralaminar damage evolution in the bricks;
2. Cohesive viscosity, regularizing damage evolution across surface-based cohesive interfaces; and
3. Automatic static-step stabilization (`*STATIC, STABILIZE`), introducing artificial viscous damping at the analysis-step level.

Each mechanism is controlled independently and can be deactivated without altering the settings of the others.

Table 3 summarizes the global energy outputs monitored during numerical assessment. Each numerical contribution `ALLX` is normalized relative to the total internal energy (`ALLIE`) as a percentage ratio:

$$R_X = 100 \times \frac{\texttt{ALLX}}{\texttt{ALLIE}}. \tag{5}$$

Ratios are evaluated only after `ALLIE` exceeds a non-zero threshold to prevent spurious energy spikes at the onset of loading. For automatic static-step stabilization, an upper screening limit of $R_{\mathrm{SD}} \leq 5\%$ is enforced, with values substantially below 1% preferred [24]. Although no universal threshold exists for viscous dissipation (`ALLCD`), its influence is verified by ensuring that further viscosity reductions yield negligible changes in macroscopic force–displacement responses.

Table 3: Global energy outputs monitored during numerical assessment.

Output	Physical / Numerical Interpretation
`ALLIE`	Total internal energy (used for normalization).
`ALLSE`	Recoverable elastic strain energy.
`ALLPD`	Energy dissipated by matrix plasticity.
`ALLDMD`	Energy dissipated by bulk-material damage initiation and evolution.
`ALLCD`	Energy associated with Hashin and/or cohesive viscous damage regularization.
`ALLSD`	Energy dissipated by automatic static-step stabilization forces.
`ALLVD`	Additional viscous dissipation reported by the solver.
`ALLAE`	Artificial strain energy (monitored as a hourglassing diagnostic).

In progressive tensile models, `ALLCD` combines Hashin and cohesive viscous contributions, which cannot be separated using global history outputs alone. In initiation-only tensile models and fracture simulations (DCB and 3ENF), Hashin evolution is deactivated; `ALLCD` is therefore attributed entirely to cohesive viscous regularization.

3.3.1. Energy ratios up to maximum tensile strength

The global energy balance for the e4 baseline model was evaluated across 10, 25, and 50 mm brick lengths. Table 4 reports the macroscopic response and numerical energy ratios evaluated via Equation (5) at peak nominal stress.

Table 4: Response and numerical energy ratios at maximum tensile strength for the e4 baseline discretization.

L_{brick} (mm)	Maximum stress (MPa)	Strain at maximum (%)	R_{CD} (%)	R_{AE} (%)
10	792.5	0.853	0.000010	0.003684
25	819.6	0.771	0.001371	0.007848
50	776.5	0.689	0.0000003	0.000818

As shown in Table 4, viscous dissipation (R_{CD}) and artificial strain energy (R_{AE}) remain negligible ($< 0.01\%$) at maximum stress. History outputs confirm that numerical energy contributions remain minimal throughout the pre-peak regime, justifying the use of progressive models for determining elastic stiffness, pre-peak non-linearity, and maximum strength.

Conversely, as illustrated in Figure 6, the post-peak response exhibits numerical sensitivity: viscous dissipation rises sharply during post-peak failure in the 10 mm model, whereas the 25 mm and 50 mm simulations terminate shortly after reaching peak load. Consequently, subsequent comparisons restrict evaluation to maximum

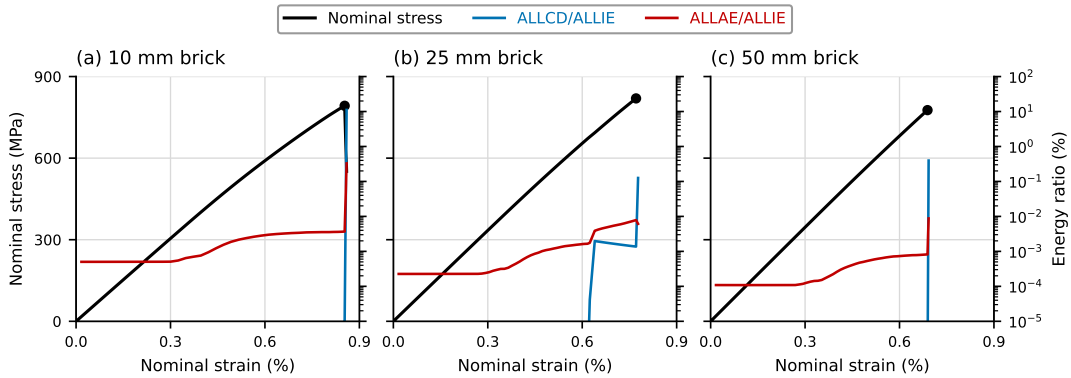

Figure 6: Nominal stress and numerical energy histories for e4 models with brick lengths of (a) 10, (b) 25, and (c) 50 mm. Black lines denote nominal stress, blue lines represent 100 ALLCD/ALLIE, and red lines represent 100 ALLAE/ALLIE. Open circles mark maximum tensile strength.

converged stress; descending branches are not considered sufficiently objective to establish residual strength or fracture energy.

3.3.2. Energy assessment of the fracture simulations

Mode I DCB and Mode II 3ENF fracture simulations require an independent energy audit due to differences in constitutive models, discretizations, and stabilization settings. Figures 7 and 8 display the load–displacement responses and energy ratios for representative 30 mm-brick configurations subjected to full loading histories. Because intralaminar Hashin evolution is deactivated in these analyses, ALLCD isolates cohesive viscous regularization. Additional monitored contributions include static-step stabilization dissipation (ALLSD) and artificial strain energy (ALLAE).

The DCB model reaches a peak load of 145.1 N at an opening displacement of 8.11 mm. At peak load, $R_{\mathrm{CD}} = 0.0032\%$, $R_{\mathrm{SD}} = 0.0320\%$, and $R_{\mathrm{AE}} = 0.2773\%$. Cohesive viscous dissipation increases during post-peak crack growth, reaching a peak ratio of approximately 0.69%. Artificial strain energy and static-step stabi-

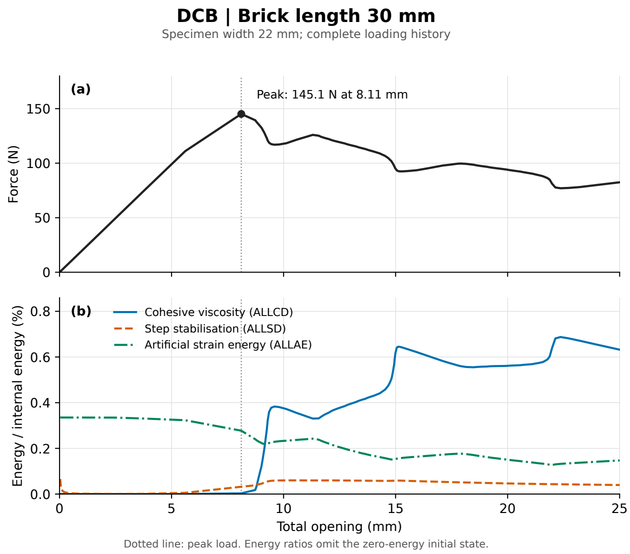

Figure 7: Numerical energy assessment of the DCB model with 30 mm bricks: (a) force versus total opening displacement and (b) cohesive viscous dissipation, static-step stabilization dissipation, and artificial strain energy normalized by internal energy. The vertical dotted line marks maximum load. Forces correspond to a specimen width of 22 mm.

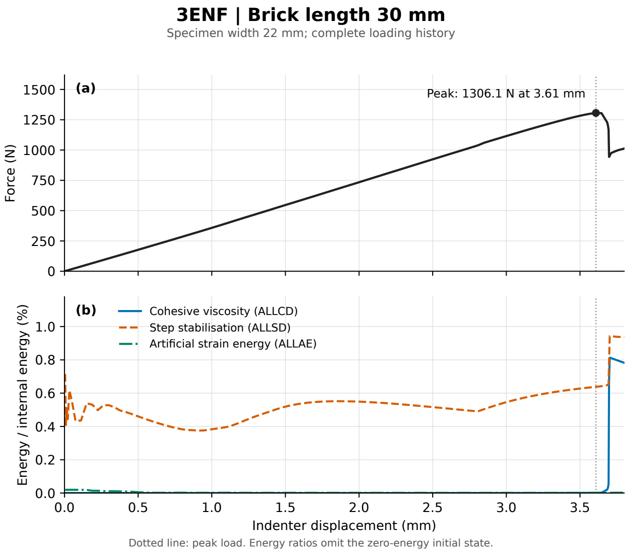

Figure 8: Numerical energy assessment of the 3ENF model with 30 mm bricks: (a) force versus indenter displacement and (b) cohesive viscous dissipation, static-step stabilization dissipation, and artificial strain energy normalized by internal energy. The vertical dotted line marks maximum load. Forces correspond to a specimen width of 22 mm.

lization dissipation remain below 0.34% and 0.066%, respectively, throughout the simulation.

The 3ENF model reaches a maximum load of 1306.1 N at an indenter displacement of 3.61 mm. At peak load, static-step stabilization constitutes the primary numerical contribution ($R_{\mathrm{SD}} = 0.6381\%$), whereas $R_{\mathrm{CD}} = 0.0013\%$ and $R_{\mathrm{AE}} = 0.0010\%$. During post-peak shear propagation, cohesive viscous dissipation and stabilization ratios increase to peak values of 0.81% and 0.94%, respectively, while artificial strain energy remains below 0.020%.

All monitored numerical energy contributions remain strictly below 1% of internal energy across both fracture modes. These results confirm that artificial numerical damping and viscous regularization do not spuriously alter predicted peak loads or delamination propagation responses.

4. Effect of brick length and layer offset

Brick length and layer offset govern the spatial distribution of matrix pockets and the overlap domain between adjacent plies. Their mechanical influence is evaluated in this section under uniaxial tensile, Mode I double-cantilever beam (DCB), and Mode II three-point end-notched flexure (3ENF) loading conditions. Constituent properties, cohesive parameters, target mesh discretizations, and solver controls are held constant within each parametric sweep. Table A.1 defines the reference geometries, while Appendix A records the matrix damage energies applied across campaigns.

The DCB and 3ENF fracture sweeps utilize 28-ply specimens featuring a 66 mm initial pre-crack positioned between plies 14 and 15. Interfaces 13–15 provide candidate cohesive failure paths (Section 2.2.4). These analyses incorporate matrix plasticity and cohesive interface damage while deactivating intraply Hashin degradation, isolating interlaminar crack propagation from progressive fibre failure. Both fracture configurations are discretized using plane-strain 4-node reduced-integration (`CPE4R`) elements, with target element heights of 0.0417 mm within the two plies bounding the pre-crack and 0.0833 mm throughout the outer blocks.

For DCB modeling, the reference mesh comprises 187,680 elements. Equal and opposite vertical displacements of ± 12.5 mm are applied at reference points located at $x = 21$ mm, generating a total opening displacement of 25 mm. The implicit static analysis utilizes unsymmetric matrix storage, initial and minimum time increments of 10^{-5} and 10^{-8}, a maximum increment of 0.1, and a static stabilization factor of 2×10^{-6} with an adaptive tolerance of 0.05.

For 3ENF modeling, the reference mesh contains 119,136 elements. Lower support rollers located at $x = 31$ mm and 131 mm establish a 100 mm span, while a central indenter at $x = 81$ mm imposes a downward displacement of 3.8 mm. All three cylindrical rollers feature a 5 mm radius with a roller-to-specimen friction coefficient of 0.10. Contact conditions develop naturally during loading without a separate seating phase. Unsymmetric storage is enforced with initial, minimum, and maximum increments of 10^{-5}, 10^{-8}, and 10^{-2}, respectively, alongside step stabilization of 10^{-7}. Table A.3 details the cohesive traction-separation parameters and viscosity coefficients.

4.1. Effect of brick length

4.1.1. Tensile response

The tensile brick-length study compares 10, 25, and 50 mm brick geometries discretized using four elements per ply (e4 mesh) with progressive Hashin damage evolution. Each architecture incorporates 0.5 mm matrix pockets and an alternating half-pitch offset sequence. Numerical tensile strength predictions are presented in Figure 9 and Table 5, benchmarked against experimental data for the same material system [19].

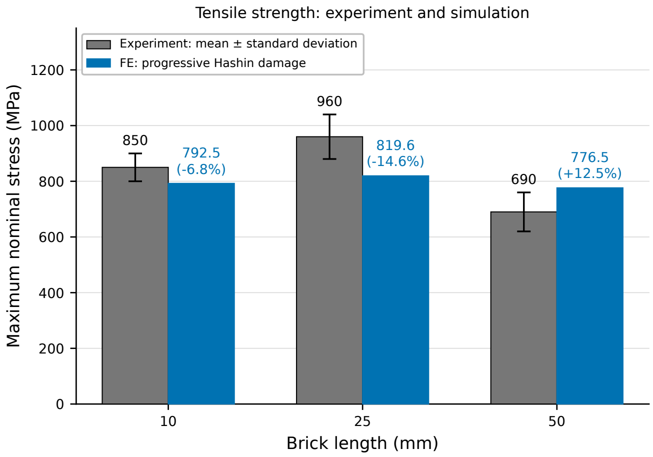

Figure 9: Maximum tensile stress of the e4 progressive Hashin models compared with experimental means and standard deviations for 10, 25, and 50 mm brick lengths [19]. Percentage labels indicate relative finite element error relative to experimental means.

Table 5: Comparison of e4 progressive tensile strength predictions against experimental measurements.

L_{brick} (mm)	Experiment (MPa)	FE maximum (MPa)	Error (%)
10	850 ± 50	792.5	-6.8
25	960 ± 80	819.6	-14.6
50	690 ± 70	776.5	$+12.5$

The numerical model underestimates experimental strength by 6.8% and 14.6% for 10 mm and 25 mm bricks, respectively, while overestimating strength by 12.5% for 50 mm bricks.

4.1.2. DCB response

Interlaminar fracture behavior was evaluated across brick lengths ranging from 10 to 50 mm at 5 mm increments. The resulting load–displacement responses in Figure 10 and maximum loads in Table 6 illustrate the influence of brick dimensions on Mode I opening and Mode II shear fracture.

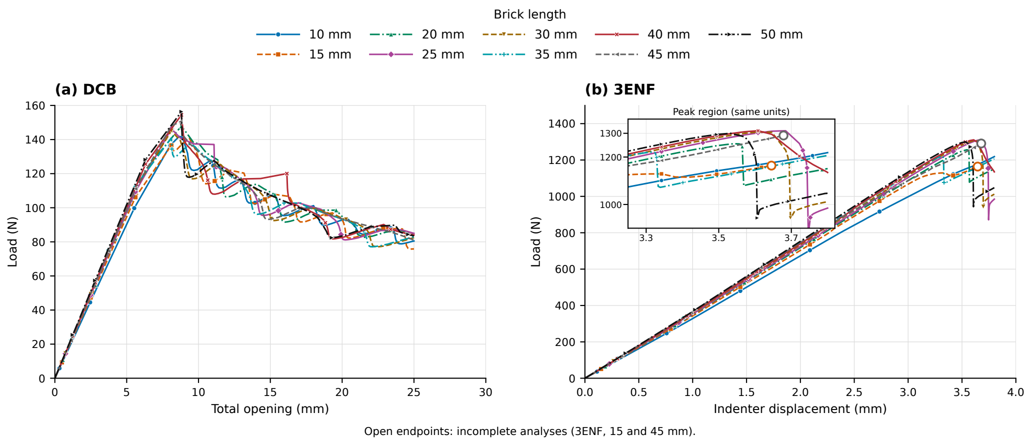

Figure 10: Effect of brick length (10 to 50 mm) on (a) DCB load versus total opening displacement and (b) 3ENF load versus indenter displacement. Open endpoint symbols denote incomplete analyses (15 mm and 45 mm 3ENF). The inset highlights the 3ENF peak load domain.

All DCB simulations successfully achieved the prescribed 25 mm opening displacement. Peak DCB loads ranged from 140.7 N (15 mm bricks) to 156.3 N (50 mm bricks), representing an 11.1% variation relative to the minimum. Intermediate brick lengths exhibited non-monotonic trends: peak load decreased between 20 mm and 35 mm before rising at 40 mm. While initial opening compliance remained insensitive to brick length, the displacement and magnitude of post-peak load drops varied systematically due to spatial shifts in matrix pocket locations

Table 6: Maximum recorded fracture loads across the brick-length parametric sweep. Parentheses designate incomplete analyses.

L_{brick} (mm)	DCB maximum (N)	3ENF maximum (N)	3ENF state
10	141.8	1218.7	Complete
15	140.7	(1163.9)	95.9%
20	148.0	1255.9	Complete
25	146.3	1310.8	Complete
30	145.1	1306.1	Complete
35	141.0	1220.9	Complete
40	154.4	1310.9	Complete
45	150.5	(1290.8)	96.9%
50	156.3	1300.0	Complete

relative to the initial crack tip. Figure 11 illustrates the transverse normal stress (S_{22}) concentration surrounding the propagating crack tip.

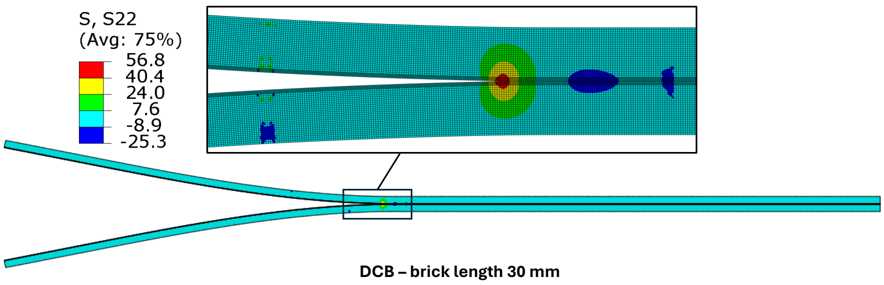

Figure 11: Transverse normal stress distribution (S_{22}, in MPa) during DCB loading for a 30 mm brick length, showing crack-tip stress concentrations.

4.1.3. 3ENF response

Completed 3ENF simulations yielded peak loads between 1218.7 N and 1310.9 N. The 25, 30, and 40 mm brick configurations achieved the highest peak loads, whereas 10 mm and 35 mm bricks produced lower maxima. This ranking contrasts with Mode I DCB testing, where 50 mm bricks sustained the highest load. The 15 mm and 45 mm 3ENF simulations terminated prematurely at 95.9% and 96.9% of total displacement; their recorded values are parenthesized in Table 6 and excluded from peak load comparisons.

Combined fracture results demonstrate that increasing brick length does not monotonically enhance structural load capacity. Because altering brick length alters the spatial offset between matrix pockets, initial crack tips, and external loading points, observed fracture performance depends heavily on the interaction between architectural geometry and loading mode. Figure 12 displays the in-plane shear stress (S_{12}) distribution during Mode II delamination.

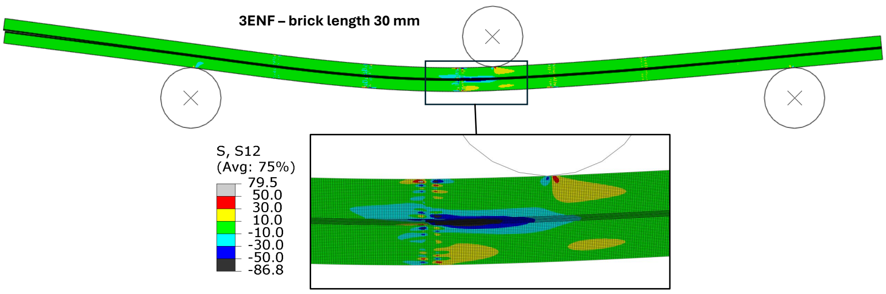

Figure 12: In-plane shear stress distribution (S_{12}, in MPa) during 3ENF loading for a 30 mm brick length, highlighting crack-tip shear stress concentration.

4.2. Effect of layer offset

4.2.1. Tensile response

The layer-offset study maintained a constant 10 mm brick length while evaluating four stacking arrangements: alternating half pitch, aligned pockets, quarter-pitch progression, and an irregular sequence.

As shown in Figure 13, layer arrangement strongly governs tensile stiffness and strength. The quarter-pitch sequence achieved the highest initial elastic modulus

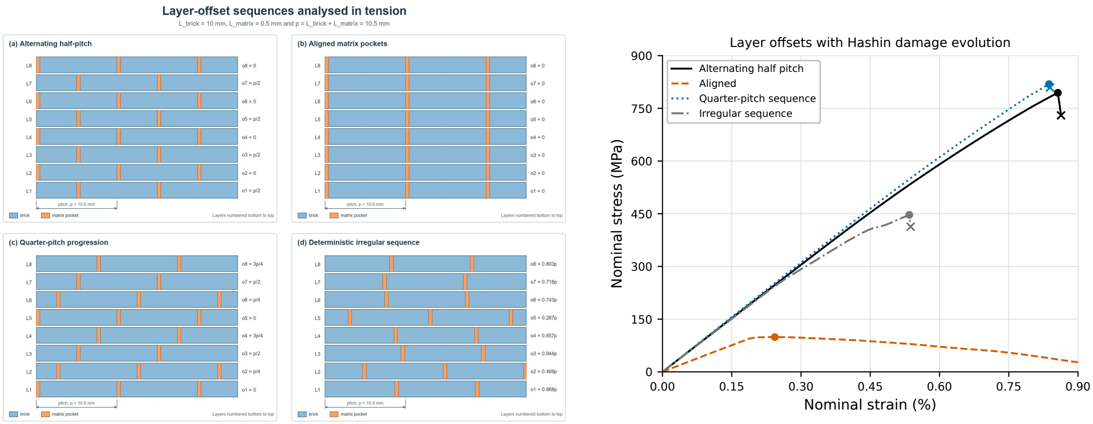

Figure 13: Layer-offset study. Left: schematic of alternating half-pitch, aligned, quarter-pitch, and irregular architectures. Right: tensile stress–strain curves incorporating progressive Hashin evolution for 10 mm bricks, 0.5 mm matrix pockets, 8 plies, and e4 mesh. Symbols denote stress maxima (circles) and final converged increments (crosses).

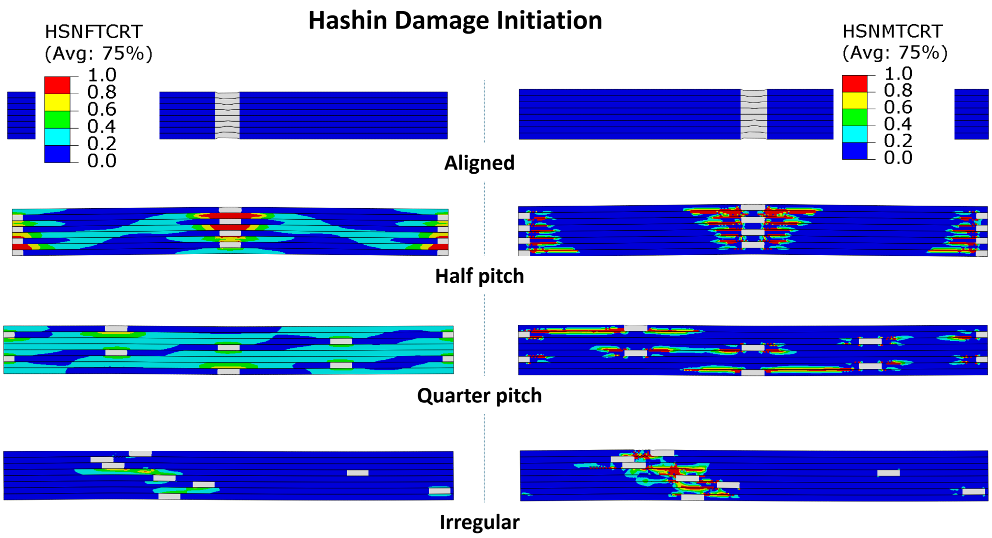

Figure 14: Hashin damage initiation distributions: fibre tension (left) and matrix tension (right) evaluated at identical nominal strain.

(103.9 GPa) and ultimate strength (818.9 MPa), compared to 101.8 GPa and 794.2 MPa for alternating half-pitch offsets. The irregular sequence retained a high initial modulus (100.6 GPa) but exhibited premature damage localization, limiting maximum stress to 446.8 MPa.

Completely aligned pockets severely compromised performance, reducing initial modulus to 50.5 GPa and maximum stress to 98.8 MPa. Aligning pockets creates continuous, transverse matrix-rich planes through the laminate thickness, forming highly compliant channels that concentrate plastic strain and damage. Offsetting pockets breaks up these continuous soft channels, redistributing load through shear stress transfer across adjacent bricks (Figure 14).

4.2.2. DCB response

The four layer-offset sequences were evaluated in 28-ply fracture specimens utilizing 25 mm bricks.

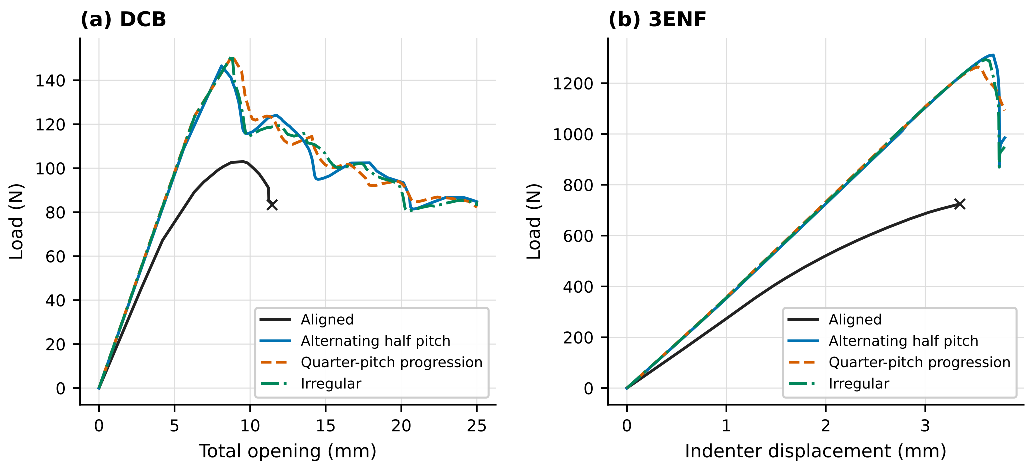

Figure 15: Influence of layer-offset sequence on (a) DCB load versus opening displacement and (b) 3ENF load versus indenter displacement for 25 mm bricks. Crosses mark terminal points of incomplete aligned simulations.

Table 7: Layer-offset comparison for Mode I DCB and Mode II 3ENF fracture simulations.

Sequence	DCB maximum (N)	3ENF maximum (N)
Aligned	103.0	724.6
Alternating half pitch	146.6	1310.8
Quarter-pitch progression	151.1	1264.0
Irregular	151.5	1293.1

Completed DCB simulations exhibited similar peak opening loads: 146.6 N for alternating half pitch, 151.1 N for quarter-pitch progression, and 151.5 N for the irregular sequence (Table 7), representing a 3.3% spread relative to the alternating baseline. Conversely, aligned matrix pockets resulted in significantly increased compliance and a substantially lower peak load of 103.0 N (Figure 15).

4.2.3. 3ENF response

In 3ENF shear fracture tests, alternating half-pitch offsets sustained the highest peak load (1310.8 N), followed by the irregular sequence (1293.1 N) and quarter-pitch progression (1264.0 N). These peak loads varied by only 3.7%, though their relative ranking differed from DCB opening response. Layer arrangement exercised a stronger influence on post-peak softening behavior, with load drops ranging from 13.6% to 33.5%. The aligned sequence again exhibited the lowest mechanical performance (724.6 N peak load).

Optimal architectural parameters depend on the dominant loading mode and performance criteria. While 25 mm bricks provided maximum tensile strength among tested lengths, 50 mm bricks sustained the highest Mode I DCB peak load. Similarly, quarter-pitch offsets maximized tensile strength, whereas alternating half-pitch offsets yielded the highest Mode II 3ENF peak load. These findings highlight the necessity of tailoring brick dimensions and offset sequences to specific structural loading environments rather than relying on a single universal architectural configuration.

5. Discussion and Conclusions

The developed scripts provide a repeatable framework for investigating the tensile and fracture responses of staggered brick-and-matrix composites. Two tensile scripts generate periodic-cell and finite-gauge models, while dedicated DCB and 3ENF scripts generate Mode I and Mode II fracture specimens. Three `Abaqus/CAE` plug-ins reproduce the principal model definitions as editable native models. Together, these tools support systematic domain verification, mesh assessment, experimental comparison, and architectural optimization.

For the baseline architecture examined, the differences in initial elastic modulus and maximum tensile stress between the single-period unit cell and the eight-period finite-gauge specimen are only 0.42% and 2.63%, respectively. This close agreement supports the use of a computationally efficient unit cell with longitudinal periodic boundary conditions to predict elastic stiffness and pre-peak strength, despite the non-linearities associated with damage initiation.

The mesh-sensitivity study demonstrates that activating intralaminar Hashin damage evolution introduces severe discretization dependence in predicted ultimate stress. Conversely, non-local initiation-only post-processing criteria eliminate softening-induced mesh dependence. The full-ply and half-ply connected-band criteria yield the closest agreement with experimental test data, whereas the enriched-ply spatial averaging criterion provides maximum objectivity against mesh refinement ($< 0.60\%$ variation).

The global energy audit confirms that viscous regularization (`ALLCD`), artificial strain energy (`ALLAE`), and static stabilization (`ALLSD`) remain negligible ($< 1\%$ of internal energy) prior to peak load across all evaluated models. However, the sharp increase in `ALLCD` during post-peak load shedding highlights that descending load–displacement branches require careful verification before extracting residual strength or fracture energy.

Parametric architectural sweeps demonstrate that altering brick length changes load-transfer paths, resulting in a non-monotonic tensile strength response. Layer offset alignment exerts an even stronger effect: continuous transverse matrix channels severely reduce both initial elastic modulus (50.5 GPa vs. 101.8 GPa) and peak tensile capacity (98.8 MPa vs. 794.2 MPa) by localizing plastic deformation.

Interlaminar fracture simulations show similar sensitivity to matrix pocket locations relative to crack tips and loading points. Changing brick length shifts crack propagation events, producing non-monotonic peak load trends. Among non-aligned offset sequences, peak loads vary within narrow bands (3.3% in DCB and 3.7% in 3ENF), whereas post-peak load drop and crack propagation paths display pronounced structural variations. Fully aligned architectures consistently exhibit degraded mechanical performance across both fracture modes.

These conclusions are specific to the material properties, geometries, boundary conditions, and solver controls evaluated within this two-dimensional framework. Applying these findings to alternative composite architectures requires repeating numerical verification and experimental validation rather than assuming universal transferability. The automated framework established here directly enables such systematic investigations.

Data availability

The Staggering model-generation scripts, Abaqus/CAE plug-ins, postprocessing evaluators, selected processed numerical datasets, and associated documentation are publicly available at https://github.com/ResearchIdea/Staggering-software. The postprocessing collection is located in `postprocessing/ply_criteria` and includes full-, half-, quarter-, and enriched-ply criteria, comparison scripts, reference data, and usage instructions. Abaqus output databases and the complete simulation campaign outputs are not publicly available.

Acknowledgments

The author acknowledges the University of Salamanca for institutional support.

Declaration of competing interest

The author declares no conflicts of interest.

A. Reference model parameters

This appendix collects the reference geometries, discretisations, constituent properties and cohesive parameters used in the numerical applications. Case-specific changes are identified in the corresponding studies.

A.1. Geometry and discretisation

Table A.1 lists the reference configurations. All plies are 0.14 mm thick. Unless stated otherwise, successive plies alternate between offsets of 0 and $p/2$, and brick material direction 1 follows the longitudinal axis. DCB and 3ENF reactions from the unit-thickness models are scaled to a specimen width of 22 mm.

Table A.1: Reference geometries and discretisations.

Model	Formulation	Length (mm)	Plies	Thickness (mm)	$L_{\text{brick}}/L_{\text{matrix}}$ (mm)	Mesh size (mm)
Tension	CPS4R, plane stress	10.5 / 84.5[a]	8	1.12	10/0.5	0.035
DCB	CPE4R, plane strain	230	28	3.92	25/0.5	0.0417 / 0.0833
3ENF	CPE4R, plane strain	146	28	3.92	25/0.5	0.0417 / 0.0833

[a] One-period longitudinally periodic cell / eight-period finite-gauge specimen. The finite gauge includes an additional 0.5 mm matrix-pocket allowance at its ends:
$L = 8p + L_{\text{matrix}} = 84.5$ mm.

A.2. Constituent and cohesive properties

Tables A.2 and A.3 specify the constituent and interface properties, including differences between the tensile and fracture-test applications.

A.3. Matrix ductile damage

The matrix damage energy requires care because Abaqus converts the softening law using the characteristic element length. Approximating the toughness density as $U_t \simeq \sigma_y \varepsilon_f$ gives $98 \times 0.30 = 29.4$ MPa. For the baseline characteristic length of 0.035 mm, the corresponding value is $G_f \simeq 1.029$ N/mm. The adopted value of 1.50 N/mm is retained as the tensile reference parameter. It is fixed throughout the tensile mesh comparisons rather than fitted separately to each mesh. The fracture brick-length sweep uses the archived value of 1.47 N/mm; the later fracture-offset and matched-route studies use 1.50 N/mm. These campaigns are therefore compared internally, not treated as identical realisations of one reference model.

Table A.2: Reference constituent properties. Elastic moduli and strengths are in MPa; fracture energies are in N/mm.

Constituent	Constitutive component	Parameters
Brick	Orthotropic elasticity	$E_1/E_2/E_3 = 120000/9000/9000$; $\nu_{12}/\nu_{13}/\nu_{23} = 0.30/0.30/0.40$; $G_{12}/G_{13}/G_{23} = 3500/3500/2000$
Brick	Hashin initiation	$X_t/X_c/Y_t/Y_c/S_L/S_T = 1860/1489/105/250/70/70$
Brick	Hashin evolution	$G_{ft}/G_{fc}/G_{mt}/G_{mc} = 80/100/1/1$; viscosities $10^{-5}/5 \times 10^{-5}/5 \times 10^{-5}/5 \times 10^{-5}$
Matrix	Isotropic elasticity and plasticity	$E = 4000$, $\nu = 0.30$; $(\sigma_y, \bar{\varepsilon}^p) = (98, 0)$ and $(101, 0.045)$ in tension, with the second plastic strain set to 0.04 in DCB and 3ENF
Matrix	Ductile damage	Initiation at $\bar{\varepsilon}^p = 0.30$, stress triaxiality 0.333 and strain rate 0; energy-based evolution with $G_f = 1.50$ in tension and the fracture-offset study, and $G_f = 1.47$ in the archived fracture brick-length sweep

Table A.3: Reference surface-based cohesive properties.

Property	Tension	DCB	3ENF
$K_{nn}/K_{ss}/K_{tt}$ (MPa/mm)	$10^6/10^6/10^6$	$10^4/10^4/10^4$	$10^4/10^4/10^4$
Initiation	Maximum nominal stress	Quadratic nominal stress	Quadratic nominal stress
$t_n^0/t_s^0/t_t^0$ (MPa)	118/144/144	60/80/80	60/80/80
Evolution	Linear, energy based, BK 1.5	Linear, energy based, BK 1.5	Linear, energy based, BK 1.5
$G_I/G_{II}/G_{III}$ (N/mm)	1.76/3.00/3.00	1.50/3.00/3.00	1.76/3.00/3.00
Reference viscosity	5×10^{-5}	2×10^{-5}	2×10^{-5}

B. Cross-route implementation verification

Matched 25 mm-brick models were generated through the standalone and native routes using equal parameter dictionaries. Table B.1 reports the semantic and numerical checks. Each pair has the same element count. The two tensile curves agree to numerical precision over their common converged interval. The DCB and 3ENF peak-load differences are 0.016 and 0.007%, respectively. DCB curve NRMSE is larger, 0.406%, because discrete crack-growth drops shift slightly despite almost identical peak and work.

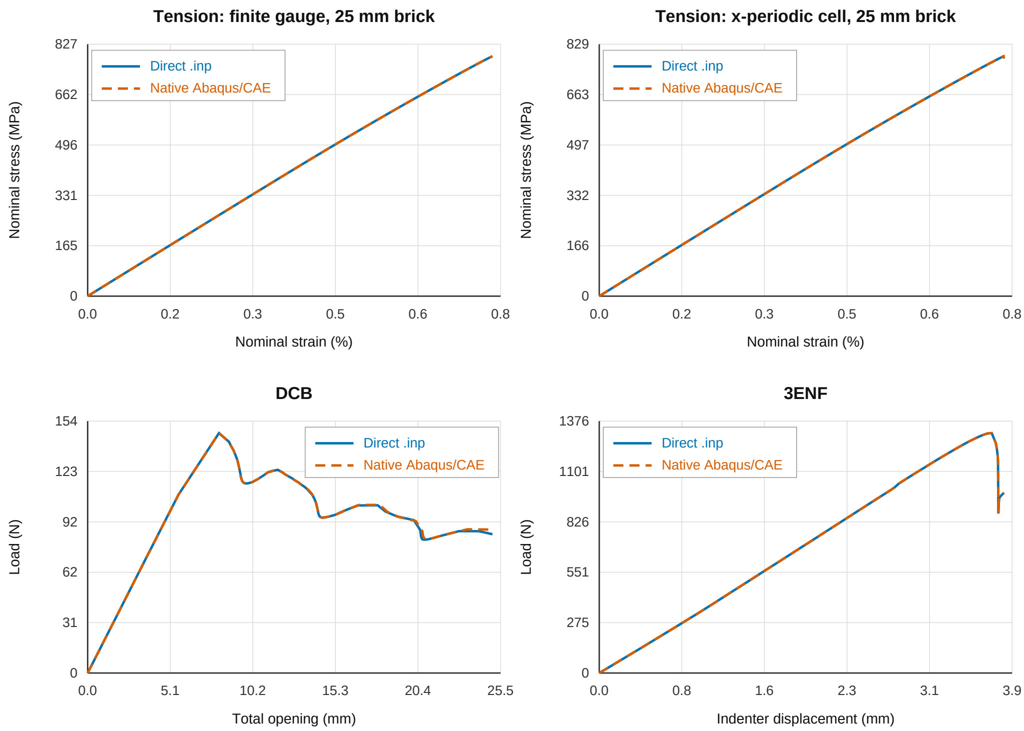

Figure B.1: End-to-end comparison of matched standalone and native models. The comparison verifies implementation consistency and is not presented as a separate physical validation.

The final step times of the tensile pairs show that both progressive-damage analyses terminate after passing their maximum load; the comparison is limited to

Table B.1: Matched route-verification cases. Differences are calculated over the common converged interval.

Case	N_e	NRMSE (%)	Peak diff. (%)	Work diff. (%)	Final step time
Finite-gauge tension	23744	1.1×10^{-6}	0.000	6.5×10^{-7}	0.831 / 0.831
Periodic tension	23296	1.8×10^{-6}	6.9×10^{-6}	1.3×10^{-6}	0.820 / 0.821
DCB	187680	0.406	0.016	0.203	1.000 / 1.000
3ENF	119136	0.0045	0.0072	0.0030	1.000 / 1.000

the common converged response. Route verification confirms equal implementation of the chosen model. This implementation check is distinct from the experimental comparison in Section 4.1.1.

C. Standalone generator command reference

The four standalone generators use only the Python standard library. Each can be run with Python 2.7 or Python 3, and every argument is optional. Omitting an argument retains the value stored in the script's `DEFAULTS` or `P` dictionary. The complete help for a generator is displayed with `-help`, for example:

```
python generate_tensile_periodic_inp.py --help
```

Tables C.1–C.3 list the published command-line interfaces. Options separated by a slash are mutually exclusive. The progressive tensile calculations use --hashin, which activates Hashin initiation and energy-based damage evolution; --no-hashin omits the Hashin model entirely. The spatial-screening study starts from a --hashin input file. A separate initiation-only copy is prepared by removing the brick-material damage-evolution and damage-stabilisation blocks while retaining Hashin initiation and its field outputs, as described in Appendix C.1.

Table C.1: Command-line options shared by the periodic and finite-gauge tensile generators.

Group	Arguments	Function
Files and formulation	--out-file, --job-name, --analysis-type	Set the output path, job name and plane-stress or plane-strain formulation.
Architecture	--ply-thickness, --n-plies, --brick-length, --matrix-pocket-length, --continuous-plies/--matrix-pockets, --n-periods-x, --layer-offsets, --ply-angles	Define the specimen, repeated cells, material pockets, layer sequence and brick orientations.
Mesh and load	--elements-per-ply, --imposed-ux	Set the through-ply mesh density and prescribed positive tensile extension.
Brick and matrix damage	--hashin/--no-hashin, --max-degradation, --matrix-damage-energy, --matrix-E, --matrix-nu	Activate progressive Hashin damage, set residual-stiffness control and define the exposed matrix properties.
Cohesive law	--Knn, --Kss, --Ktt, --tn0, --ts0, --tt0, --GIc, --GIIc, --GIIIc, --bk-power	Set independent penalty stiffnesses, nominal strengths, fracture energies and the Benzeggagh–Kenane exponent.
Solution controls	--linear/--nlgeom, --unsymmetric-matrix/--symmetric-matrix, --time-incrementation-controls/--default-time-incrementation-controls, --initial-increment, --minimum-increment, --maximum-increment, --maximum-increments	Control geometric nonlinearity, equation storage and static-step increments.
Regularisation	--cohesive-viscosity, --cohesive-stabilization/--no-cohesive-stabilization, --step-stabilization/--no-step-stabilization, --step-stabilization-factor, --adaptive-damping-ratio	Control cohesive viscous regularisation and static-step stabilisation independently.
Output	--field-frequency, --history-time-interval, --exact-time-marks/--no-exact-time-marks, --node-field-variables, --element-field-variables, --contact-field-variables, --energy-history-variables, --rp-history-variables	Select field and history intervals, exact marks and requested variables.

Table C.2: Command-line options of `generate_dcb_inp.py`.

Group	Arguments	Function
Files and formulation	--out-file, --job-name, --analysis-type	Set the output path, job name and plane-strain or plane-stress elements.
Architecture	--length, --full-specimen-length, --width, --n-layers, --layer-thickness, --brick-length, --matrix-pocket-length, --continuous-plies/--matrix-pockets, --layer-offsets/--layer-offset-file	Define specimen dimensions, brick-and-matrix geometry and one offset per layer.
Crack and mesh	--initial-crack, --precrack-interface, --potential-crack-interfaces, --nx, --fine-element-size, --coarse-element-size	Define the initial delamination, candidate paths and independent central and outer mesh densities.
Material and cohesive law	--matrix-damage-energy, --cohesive-stiffness, --cohesive-softening, --cohesive-stabilizati on/--no-cohesive-stabilization, --cohesive-damage-stabilization	Set matrix damage energy, common cohesive stiffness, linear or exponential softening and cohesive viscosity.
Loading and solution	--grip-distance, --grip-rp-offset, --total-opening-displacement, --nlgeom, --main-stabilization, --unsymmetric-matrix/--symmetric-matrix, --time-incrementation-controls/--default-time-i ncrementation-controls, --linear-check	Define loading and nonlinear controls. A zero main-stabilisation factor disables step-level stabilisation; --linear-check creates a diagnostic 1 mm run.

Table C.3: Command-line options of `generate_3enf_inp.py`.

Group	Arguments	Function
Files and formulation	--out-file, --job-name, --analysis-type	Set the output path, job name and element formulation.
Architecture	--length, --full-specimen-length, --width, --n-layers, --layer-thickness, --brick-length, --matrix-pocket-length, --continuous-plies/--matrix-pockets	Define specimen dimensions and select the staggered or continuous-ply geometry.
Crack, fixture and mesh	--initial-crack, --precrack-interface, --potential-crack-interfaces, --left-support-x, --nx, --fine-element-size, --coarse-element-size	Define the delamination, candidate paths, fixture position and mesh densities.
Material and cohesive law	--matrix-damage-energy, --cohesive-stiffness, --knn, --kss, --ktt, --cohesive-softening, --cohesive-stabilization/--no-cohesive-stabilization, --cohesive-damage-stabilization	Set matrix damage energy and common or independent cohesive properties.
Loading and solution	--main-displacement, --nlgeom, --step-stabilization/--no-step-stabilization, --main-stabilization, --unsymmetric-matrix/--symmetric-matrix, --time-incrementation-controls/--default-time-incrementation-controls	Set indenter displacement, geometric nonlinearity and independent solver and step-stabilisation controls.
Output	--history-time-interval, --exact-time-marks	Set history spacing and optionally require exact output times; exact marks may force smaller increments.

C.1. Examples of input-file generation

The following examples use mm, N and MPa and are run from the directory that contains each generator. A trailing backslash denotes continuation in a POSIX shell; in Windows PowerShell it can be replaced by a backtick, or the complete command can be entered on one line. Generation writes the input file but does not start Abaqus/CAE or submit an analysis.

C.1.1. Finite-gauge tensile model

```
python generate_tensile_uniform_inp.py \
  --out-file example_tensile_uniform.inp \
  --job-name example_tensile_uniform \
  --brick-length 25 --matrix-pocket-length 0.5 \
  --n-plies 8 --n-periods-x 1 --elements-per-ply 4 \
  --imposed-ux 0.10 --max-degradation 0.95 \
  --hashin --nlgeom --unsymmetric-matrix
```

C.1.2. Longitudinally periodic tensile cell

```
python generate_tensile_periodic_inp.py \
  --out-file example_tensile_periodic.inp \
  --job-name example_tensile_periodic \
  --brick-length 25 --matrix-pocket-length 0.5 \
  --n-plies 8 --n-periods-x 1 --elements-per-ply 4 \
  --imposed-ux 0.10 --max-degradation 0.95 \
  --hashin --nlgeom --unsymmetric-matrix
```

C.1.3. Spatially averaged Hashin screening

Unlike the other generation examples, this workflow starts from the repository root. First, generate a periodic tensile input file with Hashin initiation and evolution enabled:

```
python \
  python_inp_generators/tensile/generate_tensile_periodic_inp.py \
  --out-file example_tensile_periodic.inp \
  --job-name example_tensile_periodic \
  --brick-length 25 --matrix-pocket-length 0.5 \
  --n-plies 8 --n-periods-x 1 --elements-per-ply 4 \
  --imposed-ux 0.306 --maximum-increment 0.005 \
  --hashin --nlgeom --unsymmetric-matrix
```

Create a copy named `example_tensile_periodic_init.inp`. In this copy, remove the `*DAMAGE EVOLUTION` and `*DAMAGE STABILIZATION` keyword blocks, including their associated data lines, from the brick material definition (`*MATERIAL, NAME=COMPOSITE`) only. Retain the Hashin damage-initiation definition and its output requests. Do not remove the matrix damage or cohesive-interface definitions. The --no-hashin option is unsuitable for this preparation because it removes Hashin initiation as well as evolution.

Submit the initiation-only model from the repository root:

```
abaqus job=example_tensile_periodic_init \
  input=example_tensile_periodic_init.inp cpus=1 \
  interactive ask_delete=OFF
```

Then enter the postprocessing directory and evaluate the resulting ODB:

```
cd postprocessing/ply_criteria/studies/tensile_validation

abaqus python \
  spatial_hashin_prototype/evaluate_hashin_spatial_average.py \
  -- --odb ../../../../example_tensile_periodic_init.odb \
  --json spatial_event.json --csv spatial_event.csv \
  --trace spatial_trace.csv --gauge-length 25.5 \
  --periodic-length 25.5 --radii 0.14

cd ../../../..
```

The JSON and CSV outputs are written in the postprocessing directory. The prescribed displacement corresponds to a target nominal strain of 1.2%. Confirm that the converged history reaches the screening threshold; otherwise, the failure event cannot be determined from that analysis. This example illustrates the workflow rather than reproducing the complete numerical campaign. The radius is a physical length in millimetres and must not be changed when the mesh is refined. For a different ply thickness or material system it must be calibrated and then checked against independent configurations.

C.1.4. DCB model

```
python generate_dcb_inp.py \
  --out-file example_dcb.inp --job-name example_dcb \
  --brick-length 25 --matrix-pocket-length 0.5 \
  --n-layers 28 --initial-crack 66 \
  --potential-crack-interfaces 13,14,15 \
  --cohesive-softening linear --cohesive-stabilization \
  --cohesive-damage-stabilization 2e-5 \
  --main-stabilization 2e-6 \
  --total-opening-displacement 25 --nlgeom YES
```

C.1.5. 3ENF model

```
python generate_3enf_inp.py \
  --out-file example_3enf.inp --job-name example_3enf \
  --brick-length 25 --matrix-pocket-length 0.5 \
  --n-layers 28 --initial-crack 66 \
  --potential-crack-interfaces 13,14,15 \
  --left-support-x 31 --cohesive-softening linear \
  --cohesive-stabilization \
  --cohesive-damage-stabilization 2e-5 \
  --step-stabilization --main-stabilization 1e-7 \
  --main-displacement -3.8 --nlgeom YES
```

After generation, an input file can be submitted to Abaqus/Standard separately. For example, the following command runs the periodic tensile case with one CPU and double precision:

```
abaqus job=example_tensile_periodic \
  input=example_tensile_periodic.inp cpus=1 \
  interactive ask_delete=OFF
```

The processor count and precision mode are execution choices rather than model generation parameters. The native plug-ins are instead launched from the Abaqus/CAE *Plug-ins* menu and require no shell command.

D. Enriched-ply post-processing method and script

The enriched-ply calculation is implemented in `postprocessing/ply_criteria/studies/tensile_validation/spatial_hashin_prototype/evaluate_hashin_spatial_average.py`. It is a read-only Abaqus Python postprocessor: it does not change the input file, material law, mesh or ODB. Its purpose is to replace a mesh-row-based onset definition by an index evaluated over a fixed physical neighbourhood. The supplied implementation requires `odbAccess`, NumPy, the stress field `S`, a brick element set named `BRICK_ALL` by default, and one history region that contains `U1` and `RF1`.

The script performs the following operations:

1. It opens the ODB in read-only mode and extracts the displacement and reaction histories used to reconstruct nominal strain, stress and force.
2. It reconstructs the brick-element geometry from nodal coordinates, calculating each centroid, bounding box and area. Elements are assigned to a ply from their centroid coordinate.
3. Within each ply, a union–find graph separates disconnected brick regions using shared full edges. When a periodic length is supplied, matching regions at the two longitudinal boundaries are joined.
4. For every output frame, it evaluates Eq. (3) at each integration point, with the positive-part extension described in Section 3.1.2, and retains the largest value for each brick element. The stored stress components are assumed to follow the material 1–2 directions used by the model.
5. It constructs neighbour pairs only within the same connected brick and ply. Candidate searches are accelerated with spatial bins. For each requested radius, the pair weight is

$$w_{ij}(R) = A_j \left[1 - (r_{ij}/R)^2\right]^2, \qquad r_{ij} \leq R, \tag{D.1}$$

and zero otherwise. Normalisation of these weights gives Eq. (4).

6. It locates the first frame for which the largest enriched index reaches the requested threshold. The crossing time is linearly interpolated between adjacent frames, after which `U1` and `RF1` are interpolated at the same time.
7. It writes a JSON record with the method and critical location, a CSV of first-crossing events for every radius, and a CSV trace containing the maximum local and enriched indices in every processed frame.

Table D.1 summarises the principal command-line inputs. The complete invocation used for the examples is given in Appendix C. Radii are expressed in the model length unit and must be held fixed when the mesh is refined.

The enrichment radius is not identified by the mesh study. The value $R = t$ is retained as a layer-scale trial because it is fixed in physical units and does not average beyond a single-ply length scale. It must nevertheless be calibrated once and checked against independent geometries before the enriched criterion is used as a predictive failure model. The current script evaluates fibre-tension initiation only; it does not provide stiffness degradation, post-peak evolution or a mixed-mode intralaminar criterion for DCB and 3ENF.

References

[1] Soutis, C. Fibre reinforced composites in aircraft construction. *Prog. Aerosp. Sci.* **2005**, *41*, 143–151. https://doi.org/10.1016/j.paerosci.2005.02.004.

[2] Camanho, P.P.; Dávila, C.G. *Mixed-Mode Decohesion Finite Elements for the Simulation of Delamination in Composite Materials*; NASA/TM-2002-211737; NASA Langley Research Center: Hampton, VA, USA, 2002. Available online: https://ntrs.nasa.gov/citations/20020053651 (accessed on 4 September 2026).

Table D.1: Principal inputs and outputs of the enriched-ply postprocessor.

Argument	Purpose
--odb	Abaqus output database opened in read-only mode.
--json, --csv, --trace	Metadata, first-crossing events and frame-by-frame diagnostic output.
--radii	Comma-separated physical averaging radii; the reference study includes $R = t = 0.14$ mm.
--threshold	Enriched-index threshold, equal to 1 by default.
--ply-thickness, --brick-set	Ply classification and selection of brick elements.
--gauge-length, --total-thickness, --out-of-plane-thickness	Conversion of displacement and reaction into nominal strain, nominal stress and force.
--periodic-length	Minimum-image distance across longitudinal periodic boundaries; zero disables periodic wrapping.
--fibre-tensile-strength, --longitudinal-shear-strength, --hashin-alpha	Parameters used to reconstruct the instantaneous fibre-tension index.
--verify-abaqus-index	Optionally records the maximum Abaqus `HSNFTCRT` value for a diagnostic comparison.

[3] Swolfs, Y.; Gorbatikh, L.; Verpoest, I. Fibre hybridisation in polymer composites: A review. *Compos. Part A Appl. Sci. Manuf.* **2014**, *67*, 181–200. https://doi.org/10.1016/j.compositesa.2014.08.027.

[4] Vallack, N.; Sampson, W.W. Materials systems for interleave toughening in polymer composites. *J. Mater. Sci.* **2022**, *57*, 6129–6156. https://doi.org/10.1007/s10853-022-06988-1.

[5] Mouritz, A.P. Review of z-pinned composite laminates. *Compos. Part A Appl. Sci. Manuf.* **2007**, *38*, 2383–2397. https://doi.org/10.1016/j.compositesa.2007.08.016.

[6] Muñoz, R.; Seltzer, R.; Martínez, V.; González, C.; Llorca, J. A material selection approach for protecting carbon/epoxy laminates against single and repeated low-velocity impacts. *Int. J. Impact Eng.* **2024**, *186*, 104893. https://doi.org/10.1016/j.ijimpeng.2024.104893.

[7] Muñoz, R.; González, C.; Llorca, J. Mechanisms of in-plane shear deformation in hybrid three-dimensional woven composites. *J. Compos. Mater.* **2015**, *49*, 3755–3763. https://doi.org/10.1177/0021998314568333.

[8] Gao, H.; Ji, B.; Jäger, I.L.; Arzt, E.; Fratzl, P. Materials become insensitive to flaws at nanoscale: Lessons from nature. *Proc. Natl. Acad. Sci. USA* **2003**, *100*, 5597–5600. https://doi.org/10.1073/pnas.0631609100.

[9] Barthelat, F.; Tang, H.; Zavattieri, P.D.; Li, C.M.; Espinosa, H.D. On the mechanics of mother-of-pearl: A key feature in the material hierarchical structure. *J. Mech. Phys. Solids* **2007**, *55*, 306–337. https://doi.org/10.1016/j.jmps.2006.07.007.

[10] Barthelat, F.; Yin, Z.; Buehler, M.J. Structure and mechanics of interfaces in biological materials. *Nat. Rev. Mater.* **2016**, *1*, 16007. https://doi.org/10.1038/natrevmats.2016.7.

[11] Pimenta, S.; Robinson, P. An analytical shear-lag model for composites with “brick-and-mortar” architecture considering non-linear matrix response and failure. *Compos. Sci. Technol.* **2014**, *104*, 111–124. https://doi.org/10.1016/j.compscitech.2014.09.001.

[12] Rodríguez-García, V.; Guzmán de Villoria, R. Automated manufacturing of bio-inspired carbon-fibre reinforced polymers. *Compos. Part B Eng.* **2021**, *215*, 108795. https://doi.org/10.1016/j.compositesb.2021.108795.

[13] Rodríguez-García, V.; Herráez, M.; Martínez, V.; Guzmán de Villoria, R. Interlaminar and translaminar fracture toughness of automated manufactured bio-inspired CFRP laminates. *Compos. Sci. Technol.* **2022**, *219*, 109236. https://doi.org/10.1016/j.compscitech.2021.109236.

[14] Abass, H.; Goutianos, S.; Qian, C.; Wilson, P.; Reynolds, N.; Peijs, T. A failure mechanics study of aligned brick-and-mortar discontinuous long-fibre composites. *J. Thermoplast. Compos. Mater.* **2026**, *39*, 2977–3007. https://doi.org/10.1177/08927057251351555.

[15] Kammara, N.V.; Muliana, A. Microstructural characteristics and its role in load transfer within staggered architectures of brittle and compliant constituents. *Int. J. Eng. Sci.* **2026**, *221*, 104476. https://doi.org/10.1016/j.ijengsci.2026.104476.

[16] Jiang, P.; Xia, G.; Bai, S.; Xu, D.; Qi, J.; Xiong, X.; Ren, X.; Li, Y. The stress transfer mechanism of nacre-like composites under off-axis tensile loading. *Acta Mech. Sin.* **2026**, *42*, 424547. https://doi.org/10.1007/s10409-024-24547-x.

[17] Bai, J.; Dong, Z.; Wang, G.; Shen, Z.; Jia, Z. Topological toughening mechanism of soft staggered composites. *Extreme Mech. Lett.* **2026**, *84*, 102473. https://doi.org/10.1016/j.eml.2026.102473.

[18] Wang, Z.; Kocich, R.; Zou, M.; Batey, D.; Spink, M.; Kunčická, L. Interfacial porosity modulates fracture of brick-and-mortar multi-metal composites in additive

manufacturing. *Compos. Part B Eng.* **2026**, *322*, 113751. https://doi.org/10.1016/j.compositesb.2026.113751.

[19] Izquierdo-Martín, C.; Muñoz, R.; Martínez, V.; Maestro, C.; Cañibano, E.; Guzmán de Villoria, R. Tensile and interlaminar behaviour of brick-and-mortar carbon fibre thermoplastic composites. *Compos. Sci. Technol.* **2026**, *285*, 111798. https://doi.org/10.1016/j.compscitech.2026.111798.

[20] ASTM International. *ASTM D5528/D5528M-21: Standard Test Method for Mode I Interlaminar Fracture Toughness of Unidirectional Fiber-Reinforced Polymer Matrix Composites*; ASTM International: West Conshohocken, PA, USA, 2021. https://doi.org/10.1520/D5528_D5528M-21.

[21] ASTM International. *ASTM D7905/D7905M-19e1: Standard Test Method for Determination of the Mode II Interlaminar Fracture Toughness of Unidirectional Fiber-Reinforced Polymer Matrix Composites*; ASTM International: West Conshohocken, PA, USA, 2019. https://doi.org/10.1520/D7905_D7905M-19E01.

[22] Alfano, G.; Crisfield, M.A. Finite element interface models for the delamination analysis of laminated composites: Mechanical and computational issues. *Int. J. Numer. Methods Eng.* **2001**, *50*, 1701–1736. https://doi.org/10.1002/nme.93.

[23] Turon, A.; Dávila, C.G.; Camanho, P.P.; Costa, J. An engineering solution for mesh size effects in the simulation of delamination using cohesive zone models. *Eng. Fract. Mech.* **2007**, *74*, 1665–1682. https://doi.org/10.1016/j.engfracmech.2006.08.025.

[24] Dassault Systèmes Simulia Corp. *Abaqus 2025 Documentation: Solving Nonlinear Problems*; Dassault Systèmes Simulia Corp.: Providence, RI, USA, 2025. Available online: https://docs.software.vt.edu/abaqusv2025/English/SIMACAEANLRefMap/simaanl-c-nonlineareqns.htm (accessed on 4 September 2026).

[25] Garoz, D.; Gilabert, F.A.; Sevenois, R.D.B.; Spronk, S.W.F.; Van Paepegem, W. Consistent application of periodic boundary conditions in implicit and explicit finite

element simulations of damage in composites. *Compos. Part B Eng.* **2019**, *168*, 254–266. https://doi.org/10.1016/j.compositesb.2018.12.023.

[26] Ballard, M.K.; Whitcomb, J.D. Effective use of cohesive zone-based models for the prediction of progressive damage at the fiber/matrix scale. *J. Compos. Mater.* **2017**, *51*, 649–669. https://doi.org/10.1177/0021998316651127.

[27] Goldmann, J.; Brummund, J.; Ulbricht, V. On boundary conditions for homogenization of volume elements undergoing localization. *Int. J. Numer. Methods Eng.* **2018**, *113*, 1–21. https://doi.org/10.1002/nme.5597.

[28] Abid, N.; Mirkhalaf, M.; Barthelat, F. Discrete-element modeling of nacre-like materials: Effects of random microstructures on strain localization and mechanical performance. *J. Mech. Phys. Solids* **2018**, *112*, 385–402. https://doi.org/10.1016/j.jmps.2017.11.003.

[29] Kouznetsova, V.; Geers, M.G.D.; Brekelmans, W.A.M. Computational homogenization for non-linear heterogeneous solids. In *Multiscale Modeling in Solid Mechanics: Computational Approaches*; Imperial College Press, **2010**; pp. 1–42.

[30] Gitman, I.M.; Askes, H.; Sluys, L.J. Representative volume: Existence and size determination. *Eng. Fract. Mech.* **2007**, *74*, 2518–2534. https://doi.org/10.1016/j.engfracmech.2006.12.021.

[31] Hofman, P.; Ke, L.; van der Meer, F.P. Circular representative volume elements for strain localization problems. *Int. J. Numer. Methods Eng.* **2023**, *124*, 784–807. https://doi.org/10.1002/nme.7142.

[32] Dassault Systèmes Simulia Corp. *Abaqus 2025 Documentation: About Damage and Failure for Fiber-Reinforced Composites*; Dassault Systèmes Simulia Corp.: Providence, RI, USA, 2025. Available online: https://docs.software.vt.edu/abaqusv2025/English/SIMACAEMATRefMap/simamat-c-damagefibercomposite.htm (accessed on 4 September 2026).